Available online at www.sciencedirect.com

SciVerse ScienceDirect

Acta Materialia 60 (2012) 469–475

Acta MATERIALIA

www.elsevier.com/locate/actamat

The temperature-dependent electrical properties of $Bi_{0.5}Na_{0.5}TiO_3$–$BaTiO_3$–$Bi_{0.5}K_{0.5}TiO_3$ near the morphotropic phase boundary

Shan-Tao Zhang [a,*], Bin Yang [b,*], Wenwu Cao [b]

[a] Department of Materials Science and Engineering & National Laboratory of Solid State Microstructures, Nanjing University, Nanjing 210093, People's Republic of China

[b] Center for Condensed Matter Science and Technology, Department of Physics, Harbin Institute of Technology, Harbin 150001, People's Republic of China

Received 27 June 2011; received in revised form 5 October 2011; accepted 6 October 2011
Available online 16 November 2011

Abstract

$Bi_{0.5}Na_{0.5}TiO_3$–$BaTiO_3$–$Bi_{0.5}K_{0.5}TiO_3$ (BNT–BT–BKT) lead-free piezoceramics with compositions near the rhombohedral–tetragonal morphotropic phase boundary (MPB) were prepared and investigated. At room temperature, all ceramics show excellent electrical properties. In this study, the best properties were observed in 0.884BNT–0.036BT–0.08BKT, with the remnant polarization, bipolar total strain, unipolar strain, piezoelectric constant, and planar electromechanical coupling factor being 34.4 μC cm^{-2}, 0.25%, 0.15%, 122 pC N^{-1}, and 0.30, respectively. Detailed analysis of the temperature dependence of polarization–electric field (*P*–*E*) loops and bipolar/unipolar strain–electric field (*S*–*E*) curves of this composition revealed a ferroelectric–antiferroelectric phase transition around 100 °C. Around this temperature, there is a significant shape change in both *P*–*E* and *S*–*E* curves, accompanied by enhanced strain and decreased polarization; the largest recoverable strain reaches 0.42%. These results can be explained by the formation of antiferroelectric order and the contribution of field-induced antiferroelectric–ferroelectric phase transition to piezoelectric response. Our results indicate that BNT–BT–BKT lead-free piezoceramics can have excellent electrical properties in compositions near the MPB and also reveal some insight into the temperature dependence of the electrical performance with the MPB composition.

Keywords: Perovskites; Piezoelectricity; Ferroelectricity; Phase transformations

1. Introduction

Piezoceramics are important for many electromechanical devices, such as sensors and actuators. The most prominent and widely used piezoceramics are lead–zirconate–titanate (PZT)-based perovskite oxides. However, with the enforcement of regulations on the restriction of the use of hazardous substances in electronic devices, intensive efforts have been devoted to the search for lead-free substitutes for commercial Pb-based piezoceramics. To date, many lead-free piezoceramics has been reported; among them, perovskite lead-free solid solutions based on $BaTiO_3$ (BT), $Bi_{0.5}Na_{0.5}TiO_3$ (BNT), $K_{0.5}Na_{0.5}NbO_3$ (KNN), $Bi_{0.5}K_{0.5}TiO_3$ (BKT) are promising environmentally friendly piezoceramics [1–4]. However, these solid solutions still have some problems to be solved before they can be used commercially. The main problem for BT-based piezoceramics is the relatively low Curie temperature (T_c), which limits the working temperature range, while for KNN- and BKT-based piezoceramics, the challenge is how to reliably produce dense ceramics [4,5]. As for BNT-based piezoceramics, they generally have relative lower piezoelectric coefficient (d_{33}) and planar mode electromechanical coupling factor (k_p) than KNN-based piezoceramics, but are comparable with that of

* Corresponding authors.
E-mail addresses: stzhang@nju.edu.cn (S.-T. Zhang), binyang@hit.edu.cn (B. Yang).

1359-6454/$36.00 © 2011 Acta Materialia Inc. Published by Elsevier Ltd. All rights reserved.
doi:10.1016/j.actamat.2011.10.010

BT-based ones [2,6]. At present no lead-free piezoceramics display piezoelectric properties as good as the PZT counterparts; therefore, it has been suggested that the required piezoelectric properties are classified for different applications, and lead-free piezoceramics targeted for each application have been developed [3].

In searching for high-performance lead-free piezoceramics, the morphotropic phase boundary (MPB) between two end members with different crystal structures has been one of the main strategies. At the MPB, are more possible polarization variants are available, which leads to enhanced dielectric, ferroelectric, and piezoelectric properties [7]. Generally speaking, MPB composition of a binary system is constrained in a very narrow composition region. For example, at room temperature, the rhombohedral–tetragonal MPB of BNT–BT exists close to BNT/BT = 94/6, BNT–BKT close to BNT/BKT = 0.16–0.20, etc. [8,9]. It is interesting to note that in ternary systems, the MPB region may be extended to a wider composition range. For example, the BNT–BT–KNN ternary system keeps the rhombohedral–tetragonal MPB-like structure and properties in a much wider composition range [10]; BNT–BT–BKT ternary systems have an even wider rhombohedral–tetragonal MPB region, which is constructed by the four points P1, P2, P3 and P4, as schematically shown in Fig. 1 [3,11–14]. The compositions close to or across this MPB region show good but somewhat composition-dependent electrical and electromechanical properties [3,11–14], e.g., the reported piezoelectric coefficient (d_{33}) varies from ~100 to ~290 pC N^{-1} [3,10–13], which can be further modified through chemical doping [15,16].

For the BNT–BT–BKT ternary system, we noticed that the works reported in the literature mainly focus on compositions either along the side lines connecting two points of P1, P2, P3, and P4 [8,9,11], or across the MPB region from BNT [12,13], whereas no detailed study had been done regarding compositions within the MPB region. A systematic investigation on dielectric, ferroelectric and piezoelectric properties of compositions within the MPB region may be helpful for further optimizing and understanding of their functional properties. In addition, piezoelectric devices may work under different temperatures – from hot, like in combustion engines, to very cold, like those occurring in outer space applications – so that investigating temperature dependence of electrical and electromechanical performances is necessary for practical applications [17].

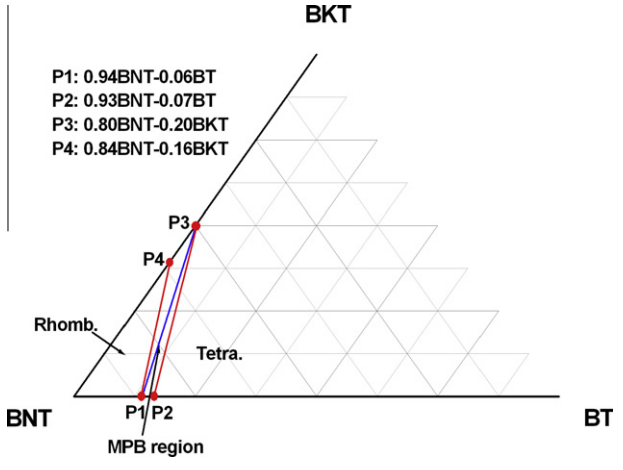

Fig. 1. The phase diagram of the BNT–BT–BKT ternary system near the BNT-rich corner. The four points (P1, P2, P3, and P4) construct the rhombohedral–tetragonal morphotropic phase boundary region. The compositions reported in this paper are located on the blue line. (For interpretation of the references to colour in this figure legend, the reader is referred to the web version of this article.)

Motivated by the above consideration, six compositions, along the blue line combining 0.94BNT–0.06BT (P1) and 0.80BNT–0.20BKT (P3) as depicted in Fig. 1, have been designed and prepared. These compositions can be described as $(0.94–0.028n)$BNT–$(0.06–0.012n)$BT–$0.04n$BKT, where $n = 0$, 1, 2, 3, 4, and 5. For $n = 0$ and $n = 5$, it is 0.94 BNT–0.06BT and 0.80BNT–0.20BKT, respectively. Room-temperature composition-dependent and temperature-dependent electrical and electromechanical properties of these compositions have been investigated and analyzed in detail.

2. Experimental procedure

Bi_2O_3 (99.8%), TiO_2 (99.0%), $BaCO_3$ (99.0%) and K_2CO_3 (99.0%), all from Sinopharm Chemical Reagent Co. Ltd., and Na_2CO_3 (99.8%) (Nanjing Chemical Reagent) were chosen as starting raw materials. For each composition, the oxides and carbonates were weighed according to the stoichiometric formula and ball milled for 24 h in ethanol. The dried slurries were calcined at 900 °C for 3 h and then ball milled again for 24 h. The powders were subsequently pressed into green disks with a diameter of 10 mm under 60 MPa. No binder was used in the pellets. Sintering was carried out at 1100 °C in covered alumina crucibles for 2 h. To reduce the volatility of Bi, Na, and K, the disks were embedded in the corresponding powder. The crystal structures of the ceramics were characterized by powder X-ray diffraction (XRD) (Rigaku Ultima III, 40 kV, 40 mA) using crushed, unpoled ceramics; the step size for the X-ray measurements was 0.03°. The microstructures were analyzed by scanning electron microscopy (SEM, FEI Quanta 200). The relative density of all samples was determined by the Archimedes method.

Electrical measurements were carried out on sintered ground circular disks with a diameter of ~8.0 mm and a thickness of ~0.45 mm. The circular surfaces of the disks were covered with a thin layer of silver paste and fired at 550 °C for 30 min. Relative dielectric constant and loss factor were measured using an impedance analyzer (HP 4294A) at several frequencies from 100 Hz to 1 MHz and over a temperature range from 50 to 350 °C. Electrical measurements were carried out at room temperature in silicone oil with controllable temperature. Polarization–electric field (P–E) ferroelectric loops and strain–electric field (S–E) curves were measured at 1 Hz in silicon oil by a Precision Premier II (Radiant Tech, USA). It is found that at high temperature, the ceramics will electrically break

down when the applied field reaches 8 kV mm^{-1}. Therefore, when carrying out the temperature-dependent electrical measurements, the applied field is fixed at a relative low field of 6 kV mm^{-1}. The piezoelectric coefficient (d_{33}) was measured by a Berlincourt-d_{33}-meter (Institute of Acoustics, Chinese Academic Society, ZJ-6A, China). With an HP 4294A impedance analyzer, the first resonance and anti-resonance frequencies of the poled ceramic disk (poling field between 6 and 7 kV mm^{-1} for 5 min) were measured and the planar electromechanical coupling factor (k_p) was evaluated based on the IEEE standards.

3. Results and discussion

3.1. XRD and SEM analysis

The XRD patterns of all compositions are depicted in Fig. 2. All sintered ceramics are crystallized into a single-phase perovskite structure. The peak positions and relative intensities of all diffraction peaks are basically the same, indicating similar crystallographic structure for all compositions, which is expected based on published phase diagrams [11–14]. Fig. 3 is the SEM micrograph of the 0.884BNT–0.036BT–0.08BKT ($n = 2$) ceramic, which is typical for all compositions. One can see that the ceramic is rather dense, with an average grain size of ~1.2 μm. It should be noted that no obvious composition dependence of grain size can be detected, which is consistent with the XRD results. The relative densities of the samples are measured to be in the range of 97.5–98.2%, and with no observable composition dependence.

3.2. Room-temperature electrical properties

3.2.1. P–E ferroelectric hysteresis

Well-saturated P–E loops can be observed in all samples. A typical loop is plotted in Fig. 4a, which is for 0.884BNT–0.036BT–0.08BKT ceramic, i.e., for $n = 2$. Note that for the case of $n = 0$, i.e., 0.94BNT–0.06BT, the ceramics usually break down when the applied field is higher than 7 kV mm^{-1}. The composition-dependent remnant polarization (P_r) and coercive field (E_c), measured

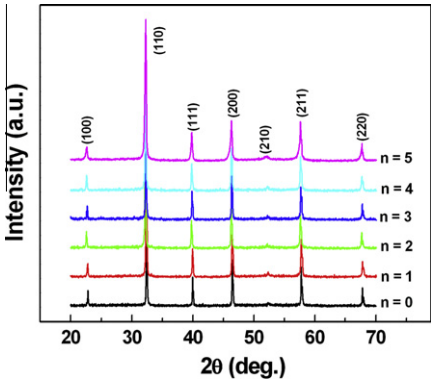

Fig. 2. X-ray diffraction patterns of all compositions investigated.

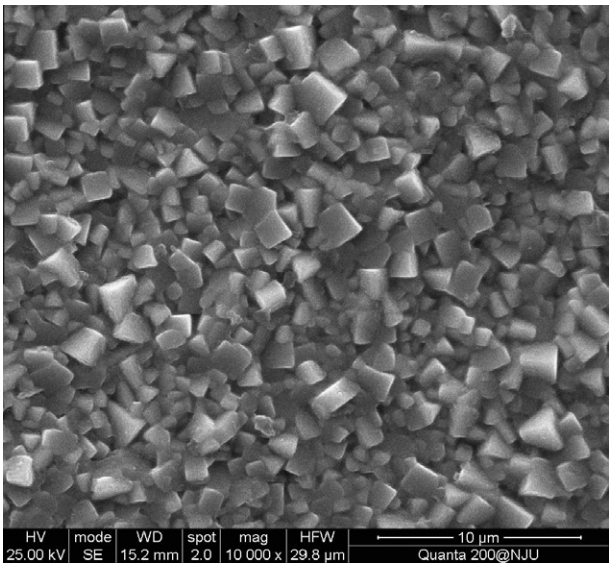

Fig. 3. Exemplary microstructure of the composition with $n = 2$ (0.884BNT–0.036BT–0.08BKT).

with the applied field up to 8 kV mm^{-1} (for 0.94BNT–0.06BT up to 7 kV mm^{-1}), are depicted in Fig. 4b. Fig. 4b clearly shows that the composition-dependent P_r has a maximum value near $n = 2$ (0.884BNT–0.036BT–0.08BKT) and a maximum value of 34.4 μC cm^{-2}. As for the coercive field E_c, the composition dependence is very limited within the range between 3.62 and 3.74 kV mm^{-1}.

As for the composition dependence of E_c and P_r, it is noted that the introduction of BKT can bring additional charged vacancies of V'_K and V'''_{Bi}, and thus $V^{\cdot\cdot}_O$ for charge compensation, these charged defects may pin the domain

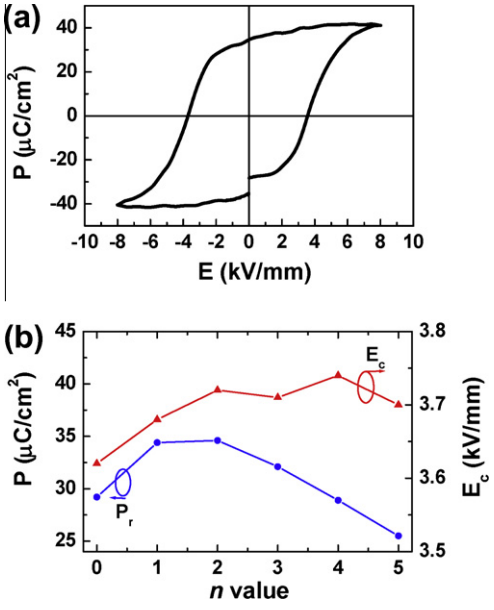

Fig. 4. (a) Room-temperature P–E ferroelectric hysteresis loop of the composition with $n = 2$ (0.884BNT–0.036BT–0.08BKT) and (b) composition-dependent P_r, and E_c.

walls, and thus tend to increase E_c, as shown in Fig. 4b. Such charged-defects-induced domain pinning also has negative effect on the P_r value. However, when n is increased from 0 to 2, this negative effect may not be dominant: the fact that the composition is approaching the core of the MPB region (which generally leads to enhanced domain switching), may be dominant, which leads to the observed increasing P_r. With further increased n from 2 to 5, the negative effect cannot be neglected: and the composition is going away from the core of MPB region, and therefore P_r decreases.

3.2.2. Bipolar and unipolar S–E curves

At room temperature, all investigated piezoceramics display typical butterfly-shaped bipolar strain–electric field (S–E) curves. The S–E curves for the composition with $n = 2$ (0.884BNT–0.036BT–0.08BKT) measured up to 8 kV mm^{-1} applied field are shown in Fig. 5a. The total strain (the difference between positive and negative maximum strain) and positive strain are plotted as a function of n in Fig. 5b. As can be seen, the strain value increases when n increases from 0 to 2 and then decreases with further increasing n. The maximum total strain and positive strain are observed to be 0.25% and 0.15%, respectively, in the 0.884BNT–0.036BT–0.08BKT ceramics. Unipolar S–E curves of this composition (0.884BNT–0.036BT–0.08BKT) are shown in Fig. 6a; the strain reaches 0.15% at 8 kV mm^{-1}. Other compositions show similar unipolar S–E curves; the composition dependence of unipolar strain values is plotted in Fig. 6b. It is noticed that at room temperature, both bipolar and unipolar strains have the same trend of composition dependence as that of the polarization (Fig. 4). This is reasonable because the strain partly comes from the contribution of ferroelectric domain switching [18].

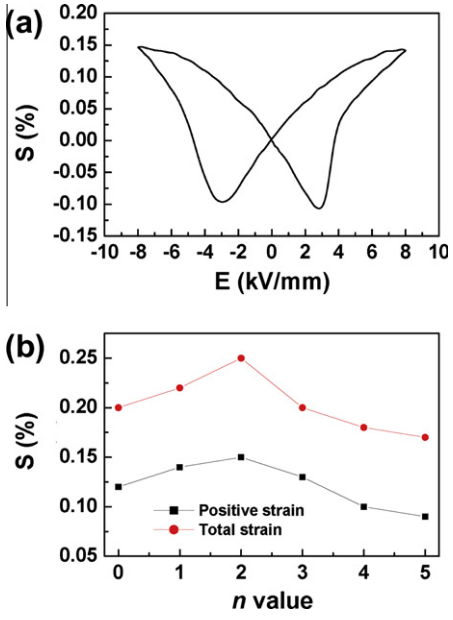

Fig. 5. (a) Room-temperature bipolar S–E curve of the composition with $n = 2$ (0.884BNT–0.036BT–0.08BKT) and (b) composition-dependent total strain and positive strain.

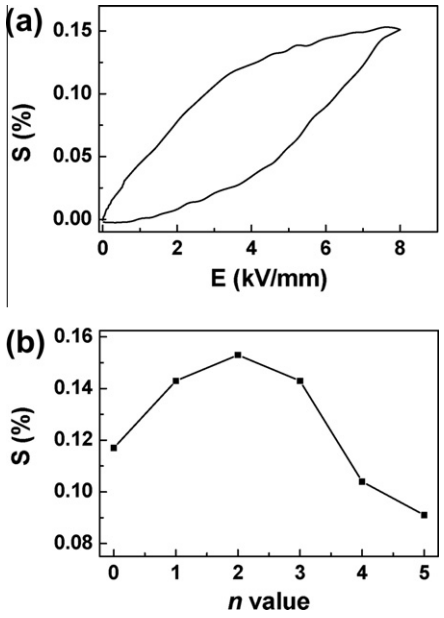

Fig. 6. (a) Room-temperature unipolar S–E curve of the composition with $n = 2$ (0.884BNT–0.036BT–0.08BKT) and (b) composition-dependent unipolar strain.

3.2.3. Piezoelectric property

As shown in Fig. 7, both the piezoelectric coefficient (d_{33}) and the planar electromechanical coupling factor (k_p) increase when n increases from 0 to 2 and then decrease monotonously with further increasing n. The d_{33} and k_p values lie in the ranges 105–122 pC N^{-1} and 0.26–0.30, respectively, with maximum values of 122 pC N^{-1} and 0.30, respectively, for the composition with $n = 2$. The trend of composition dependence of d_{33} and k_p is consistent with that of polarization and strain (Figs. 4–6) and can be explained in the same way as described above by considering the intrinsic and extrinsic contributions to piezoelectric response.

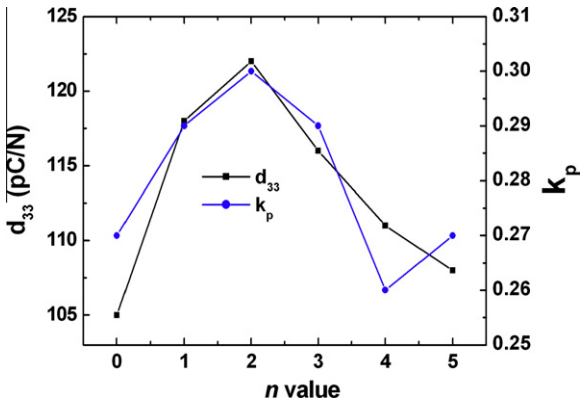

Fig. 7. Composition-dependent d_{33} and k_p.

3.3. Temperature dependence of electrical properties

3.3.1. Dielectric properties

The temperature-dependent relative permittivity (ε_r) and loss factor (tan δ) of all the unpoled samples measured at 1 kHz are shown in Fig. 8a and b, respectively. For each composition, the frequency dispersion of depolarization temperature (not shown here) and the broadness of this ε_r peak indicate a diffused phase transition, suggesting relaxor behavior of these ceramics. One can see that the temperature at the maximum of the relative dielectric constant (T_m) has no obvious composition dependence and is almost a constant near 270 °C. According to Takenaka et al. [19], it is difficult to determine the depolarization temperature (T_d) value based on the temperature dependence of dielectric properties in unpoled samples because of the rather diffused phase transition around T_d, so we propose two tangent lines on the loss factor–temperature curves to estimate the T_d [20], the as estimated T_d and the ε_r values at low temperature (e.g., 50 °C) show significant composition dependence, as shown in Fig. 9. In general, T_d decreases when n changes from 0 to 3 then begins to increase with composition, while ε_r increases slightly when n changes from 0 to 2, then begins to decrease.

3.3.2. P–E ferroelectric hysteresis

Fig. 10a shows the P–E loops of 0.884BNT–0.036BT–0.08BKT ($n = 2$) measured at different temperatures and Fig. 10b presents the temperature dependence of the averaged P_r and E_c. One can see that from room temperature to 70 °C, the loops keep the square shape and the P_r is almost a constant with the values of ~31.5 μC cm^{-2}. However, the coercive field decreases drastically from 3.1 kV mm^{-1} to 2.1 kV mm^{-1}. With further increasing temperature to 100 °C, the square loop disappears, and the P_r and E_c decreased dramatically to 9.1 μC cm^{-2} and 0.8 kV mm^{-1}, respectively. Interestingly, a pinched double hysteresis loop, which is a typical characteristic of antiferroelectrics, has been observed, in spite of the obvious remnant polarization. This P–E loop possibly means that at this temperature, the ferroelectric order tends to disappear and the antiferroelectric order tends to appear. In other words, the ferroelectric and antiferroelectric orders coexist in this system. Increasing temperature to 130 °C leads to narrower P–E loop with further decreased P_r (5.4 μC cm^{-2}) and E_c (0.6 kV mm^{-1}), which may be due to the weakening of ferroelectric order and enhanced antiferroelectric order. It is observed that further increasing temperature will cause significant leakage, preventing electrical measurements at higher temperatures.

The temperature-dependent P–E loop, and the measured P_r and E_c values, indicate the appearance of antiferroelectric order near 100 °C (which is significantly lower than the measured T_d in Fig. 9). By further noting that the shape of

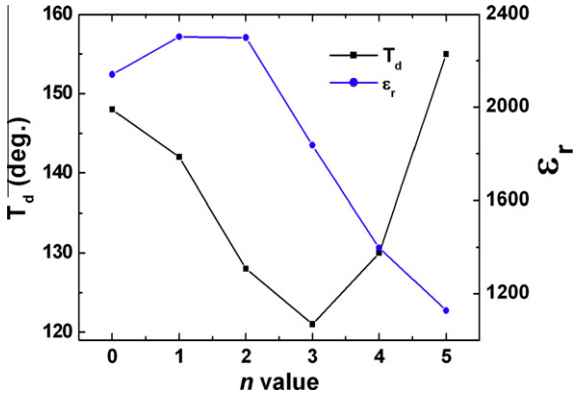

Fig. 9. Composition-dependent T_d and the ε_r values at 50 °C.

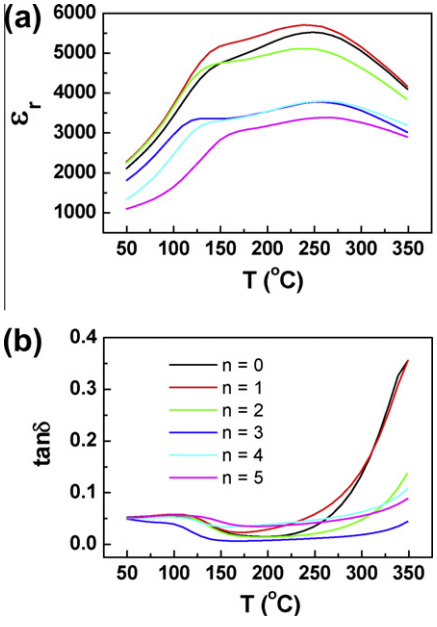

Fig. 8. Temperature-dependent (a) ε_r and (b) tan δ measured at 1 kHz for all compositions.

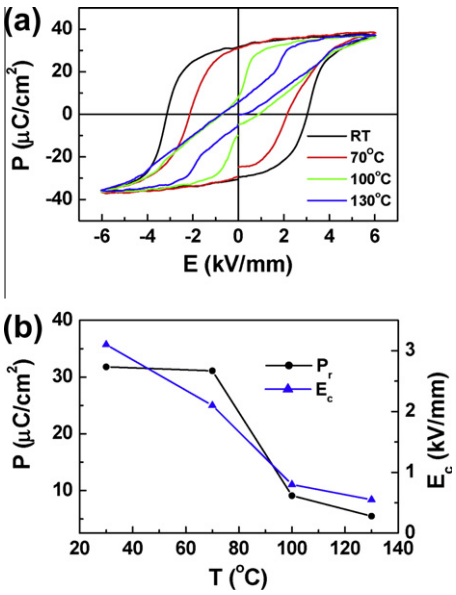

Fig. 10. (a) P–E ferroelectric hysteresis loops of the composition with $n = 2$ (0.884BNT–0.036BT–0.08BKT) at different temperatures and (b) temperature-dependent P_r and E_c.

the bipolar S–E curve above 100 °C (shown in Fig. 11) is similar to that of typical antiferroelectrics [21,22] and that BNT-based materials can have a ferroelectric–antiferroelectric phase transition around T_d [8], our results might indicate the possible appearance of antiferroelectric order, and therefore the coexistence of ferroelectric and antiferroelectric orders near 100 °C. The antiferroelectric order may be attributed to the octahedral tilt disorder, as confirmed by electron microscopy measurements [23].

3.3.3. Bipolar and unipolar S–E curves

Fig. 11a shows measured temperature-dependent bipolar S–E curves; more detailed variations of the positive strain and the total strain against temperature are plotted in Fig. 11b. As the temperature increases from room temperature to 70 °C, the S–E curves exhibit a butterfly shape, typical for ferroelectric materials. Although both the total strain and positive strain increase only slightly, the curve shape changes greatly. The positive strain increases when the temperature reaches 100 °C, while the "negative strain", which denotes the difference between zero field strain and the lowest strain, almost vanishes. These features of the bipolar S–E curves around 100 °C suggest a field-induced antiferroelectric–ferroelectric phase transition. With further increasing temperature to 130 °C, the S–E curve shows slightly decreased total strain and positive strain values. However, it should be emphasized that such temperature-dependent bipolar strain behavior is different from that of ferroelectric PZT. For PZT thin film and bulk ceramic, the maximum bipolar strain increases with increasing temperature [17,24].

We propose the following explanation for the observed temperature-dependent total strain and positive strain values. Below 70 °C, the slightly increased strain from room temperature to 70 °C is mainly attributed to a reduction of E_c, which may increase the contribution of domain switching to strain. When the temperature reaches 100 °C, there are coexisting antiferroelectric and ferroelectric orders (evidenced by the pinched ferroelectric loops); therefore strain comes mainly from the ferroelectric domain-switching component and the additional field-induced antiferroelectric–ferroelectric phase-transition component, which is generally accompanied by large strain. When the temperature is beyond 100 °C, the ferroelectric order tends to be weakened. Therefore, the strain originating from ferroelectric domain switching tends to decreases, and the total strain and positive strain tend to decrease with increasing temperature.

Fig. 12a and b shows the measured temperature-dependent unipolar strain curves and the strain values, respectively. As depicted in Fig. 12b, the maximum unipolar strain increases gradually from room temperature to 70 °C, followed by a sharp increase to 0.42% at 100 °C. The maximum unipolar strain drops slightly to 0.41% with further increasing temperature up to 130 °C. Since the unipolar strain was measured with a fixed electric field of 6 kV mm^{-1}, the temperature dependence of $d_{33} * (S_{max}/E_{max})$ is the same as that of the maximum unipolar strain. It is worth noting that the highest dynamic d_{33} is 700 pm V^{-1} at 100 °C. The temperature-dependent unipolar strain can be explained in the same way as that of bipolar strain, by considering the origin of the strain. It should be mentioned that the temperature-dependent bipolar strain and unipolar strain are consistent with the temperature dependence of P–E loops shown in Fig. 10.

4. Conclusions

$(0.94–0.028n)$BNT–$(0.06–0.012n)$BT–$0.04n$BKT ($n = 0$, 1, 2, 3, 4, and 5) lead-free piezoceramics with compositions

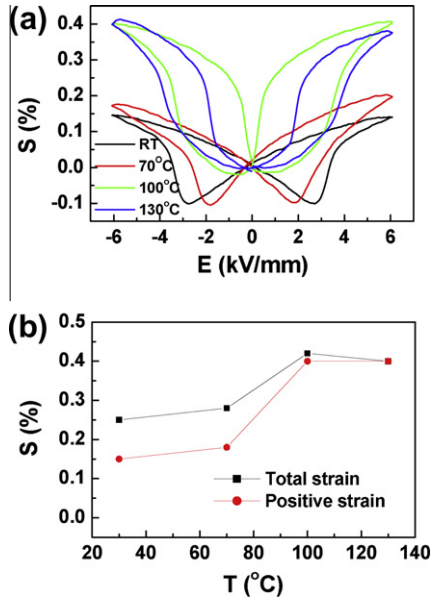

Fig. 11. (a) Bipolar S–E curves of the composition with $n = 2$ (0.884BNT–0.036BT–0.08BKT) at different temperatures and (b) temperature-dependent total strain and positive strain.

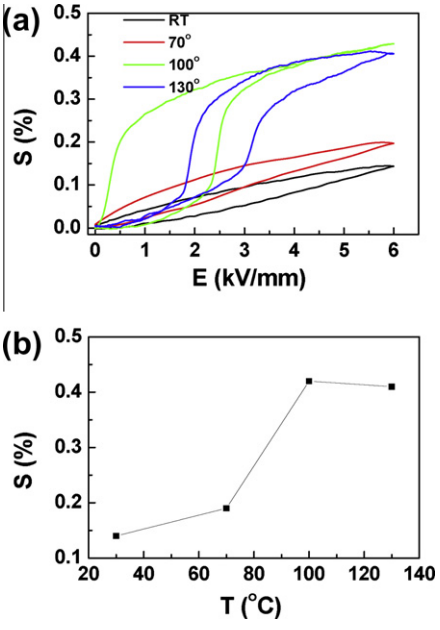

Fig. 12. (a) Unipolar S–E curves of the composition with $n = 2$ (0.884BNT–0.036BT–0.08BKT) at different temperatures and (b) temperature-dependent unipolar strain.

located in the rhombohedral–tetragonal MPB region were prepared and investigated. All ceramics show excellent but composition-dependent electrical properties at room temperature; the composition with $n = 2$ has the most optimized electrical properties. Detailed temperature dependence of *P–E* loops and bipolar/unipolar *S–E* curves of this composition reveal a ferroelectric–antiferroelectric phase transition near 100 °C. Around this temperature, both *P–E* and *S–E* curves show significant shape change, companied by enhanced strain and decreased polarization. These results can be explained by considering the intrinsic and extrinsic contributions to piezoelectric response and the effect of domain wall pinning by charged defects. Our results provided some clues for further understanding of the temperature dependence of electrical performance of BNT-based lead-free piezoceramics.

Acknowledgements

This work was supported by the National Nature Science Foundation of China (10874069 and 10704021), the Fundamental Research Funds for the Central Universities (1115021301 and 1116021301) and Natural Scientific Research Innovation Foundation in Harbin Institute of Technology (HIT.NSRIF 201055).

References

[1] Takenaka T, Nagata H. J Eur Ceram Soc 2005;25:2693.
[2] Zhang SJ, Xia R, Shrout TR. J Electroceram 2007;19:251.
[3] Takenaka T, Nagata H, Hiruma Y. Jpn J Appl Phys 2008;47:3787.
[4] Rödel J, Jo W, Seifert K, Anton E-M, Granzow T, Damjanovic D. J Am Ceram Soc 2009:921153.
[5] Hiruma Y, Nagta H, Takenaka. Jpn J Appl Phys 2007;46:1081.
[6] Saito Y, Takao H, Tani T, Nonoyama T, Takator K, Homma T, et al. Nature 2004;432:84.
[7] Cross LE. Jpn J Appl Phys 1995;34:2525.
[8] Takenaka T, Maruyama K, Sakata K. Jpn J Appl Phys 1991;30:2236.
[9] Sasaki A, Chiba T, Mamiya Y, Otsuki E. Jpn J Appl Phys 1999:385564.
[10] Zhang ST, Wang L, Chen YF, Kounga AB. J Am Ceram Soc 2010;93:1561.
[11] Nagata H, Yoshida M, Makiuchi Y, Takenaka T. Jpn J Appl Phys 2003;42:7401.
[12] Makiuchi Y, Aoyagi R, Hiruma Y, Nagata H, Takenaka T. Jpn J Appl Phys 2005;44:4350.
[13] Shieh J, Wu KC, Chen CS. Acta Mater 2007;55:3081.
[14] Hiruma Y, Nagata H, Takenaka T. Jpn J Appl Phys 2005;45:7409.
[15] Shieh J, Lin YC, Chen CS. J Phys D Appl Phys 2010;43:025404.
[16] Wang L, Song TK, Lee SC, Cho JH, Sung YS, Kim M-H, et al. Curr Appl Phys 2010;10:1059.
[17] Kungl H, Hoffmann MJ. Acta Mater 2007;55:5780.
[18] Jones JL, Hoffman M, Daniels JE, Studer AJ. Appl Phys Lett 2006;89:092901.
[19] Takenaka T, Nagata H, Hiruma Y. IEEE Trans Ultrason Ferroelectr Freq Control 2009;56:1595.
[20] Zhang ST, Kounga AB, Aulbach E, Jo W, Granzow T, Ehrenberg H, et al. J Appl Phys 2008;103:034108.
[21] Park SE, Pan M-J, Markowski K, Yoshikawa S, Cross LE. J Appl Phys 1997;82:1798.
[22] Brodeur RP, Gachigi KW, Pruna PM, Shrout TR. J Am Ceram Soc 1994;77:3042.
[23] Guo YP, Liu Y, Withers RL, Brink F, Chen H. Chem Mater 2011;23:219.
[24] Kumar P, Singh S, Thakur OP, Prakash C, Goel TC. Jpn J Appl Phys 2004;43:1501.